Check for updates

ADVANCED MATERIALS
www.advmat.de

Spatially Precise Light-Activated Dedoping in Wafer-Scale MoS_2 Films

Debjit Ghoshal, Goutam Paul, Srikrishna Sagar, Cole Shank, Lauren A. Hurley, Nina Hooper, Jeiwan Tan, Kory Burns, Jordan A. Hachtel, Andrew J. Ferguson, Jeffrey L. Blackburn, Jao van de Lagemaat, and Elisa M. Miller**

2D materials, particularly transition metal dichalcogenides (TMDCs), have shown great potential for microelectronics and optoelectronics. However, a major challenge in commercializing these materials is the inability to control their doping at a wafer scale with high spatial fidelity. Interface chemistry is used with the underlying substrate oxide and concomitant exposure to visible light in ambient conditions for photo-dedoping wafer scale MoS_2. It is hypothesized that the oxide layer traps photoexcited holes, leaving behind long-lived electrons that become available for surface reactions with ambient air at sulfur vacancies (defect sites) resulting in dedoping. Additionally, high fidelity spatial control is showcased over the dedoping process, by laser writing, and fine control achieved over the degree of doping by modulating the illumination time and power density. This localized change in MoS_2 doping density is very stable (at least 7 days) and robust to processing conditions like high temperature and vacuum. The scalability and ease of implementation of this approach can address one of the major issues preventing the "Lab to Fab" transition of 2D materials and facilitate its seamless integration for commercial applications in multi-logic devices, inverters, and other optoelectronic devices.

1. Introduction

Atomically thin semiconductors have shown a lot of promise for next generation microelectronics due to their thinness, unique layer-dependent band structure, and exceptional optoelectronic properties.[1,2] These distinctive optical and electronic properties, coupled with the ultrathin nature of layered materials, have led to various applications in flexible electronics, gas sensing, and neuromorphic computing.[3,4] While earlier efforts focused on devices from exfoliated samples, more recently, chemical vapor deposition (CVD) and metal organic chemical vapor deposition (MOCVD) techniques have led to large area wafer scale growth of monolayers of 2D materials.[5–10] This has enabled circuit scale demonstrations of field effect transistors (FETs) of the 2D monolayers for devices like ring oscillators, inverters, and logic operators.[11,12]

Although extensive efforts have focused on wafer scale growth of 2D materials, very little has been done to develop techniques to tune their carrier density using commercially feasible approaches. Having the ability to differentially dope 2D materials n- or p-type at wafer scale could enable multi-valued logic gates (>2 states) with substantially improved information density per unit area and reduced power consumption over existing technology.[13] The ability to dope these materials with high-spatial resolution forms the basis of many emerging optical and optoelectronic devices.[14,15]

D. Ghoshal, G. Paul, S. Sagar, C. Shank, N. Hooper, J. Tan, A. J. Ferguson, J. L. Blackburn, J. van de Lagemaat, E. M. Miller
Materials, Chemistry, and Computational Sciences Directorate
National Renewable Energy Laboratory
Golden, CO 80401, USA
E-mail: jao.vandelagemaat@nrel.gov; elisa.miller@nrel.gov

L. A. Hurley, J. van de Lagemaat, E. M. Miller
Renewable & Sustainable Energy Institute (RASEI)
Boulder, CO 80303, USA

L. A. Hurley
Electrical, Computer and Energy Engineering
University of Colorado Boulder
Boulder, CO 80309, USA

K. Burns
Department of Materials Science and Engineering
University of Virginia
Charlottesville, VA 22904, USA

J. A. Hachtel
Center for Nanophase Materials Sciences
Oak Ridge National Laboratory
Oak Ridge, TN 37830, USA

The ORCID identification number(s) for the author(s) of this article can be found under https://doi.org/10.1002/adma.202409825

© 2024 The Author(s). Advanced Materials published by Wiley-VCH GmbH. This is an open access article under the terms of the Creative Commons Attribution-NonCommercial License, which permits use, distribution and reproduction in any medium, provided the original work is properly cited and is not used for commercial purposes.

DOI: 10.1002/adma.202409825

15214095, 2025, 3, Downloaded from https://advanced.onlinelibrary.wiley.com/doi/10.1002/adma.202409825 by National Renewable Energy Lab, Wiley Online Library on [24/01/2025]. See the Terms and Conditions (https://onlinelibrary.wiley.com/terms-and-conditions) on Wiley Online Library for rules of use; OA articles are governed by the applicable Creative Commons License

While doping in silicon can be easily accomplished by bombarding ions of the dopant material on the silicon wafer,[16] this technique cannot be readily extended to 2D materials that are damaged by the highly energetic ion beams of the dopant material.[17] Electrostatic gating has emerged as an effective way to control doping densities in 2D materials but this comes at the cost of extensive microfabrication and is limited to two states.[18] While multiple gates can in principle result in localized control of doping, this leads to drastic increase in complexity of fabrication and therefore cost.[19,20]

More recently, efforts have focused on interfacial and chemical methods of doping graphene and transition metal dichalcogenides (TMDCs).[21,22] While these devices were good proof of concept demonstrations, the samples were fabricated by mechanical exfoliation making it unfeasible for practical implementation. Similarly, native oxidation of few layer InSe, synthesized by mechanical exfoliation was used as a novel interface to boost charge trapping, resulting in doping of the unoxidized InSe channels.[23] However, this approach is less controllable and limited to unstable materials. Dynamic doping with light and applied potential has been demonstrated in few layer $MoTe_2$ but could not be extended to other TMDCs like MoS_2 and WS_2, which are less susceptible to defect formation and more stable under illumination/applied potential.[24–26] Chemical doping in solution-processed few layer MoS_2 thin films has resulted in area-selective doping but is often unstable to processing conditions.[27] Similarly, electron beam exposure as a doping method has complexity and cost considerations.[28,29] Substitutional doping has shown promise as a scalable technique to dope large area TMDCs but this technique lacks spatial control making it less useful for fabrication of optoelectronic devices where such control is critical.[30–32] The comparison of various methods recently used for doping TMDCs is highlighted in Table S1 (Supporting Information).

We were inspired by multiple reports demonstrating variability of the optoelectronic properties of monolayer TMDCs under ambient conditions.[33–35] Due to their ultrathin nature, the electronic and optical properties of TMDCs can be extremely sensitive to the environment they are placed in. While this makes benchmarking a challenge with these materials, it also offers opportunities to modulate their properties (including doping/dedoping) provided one can unravel the salient mechanism(s).[36–39] Recent reports have shown large changes in photoluminescence (PL) of monolayer TMDCs upon exposure to light in ambient/controlled conditions.[40–45] Several studies, including ours, have linked this observation to the passivation of vacancy-related defect states through chemisorption and/or physisorption processes.[46–50] While the exact mechanism is still hotly debated, these results demonstrate the potential to photomodulate optoelectronic properties of TMDCs.

In this work, we demonstrate that the underlying oxide interface between the monolayer MoS_2 and the substrate plays a critical role in the observed enhancements in PL (under ambient conditions) upon illumination. We conclusively show with Kelvin Probe Force Microscopy (KPFM) measurements that these enhancements in PL upon illumination correlate directly to doping level changes. We leverage this idea to develop a facile approach to controllably dedope wafer scale MoS_2 with high spatial resolution that is stable for at least a week. Additionally, we show control over doping density, by tuning the time and power of illumination. This demonstration opens avenues for lithography-free fabrication of multi-logic devices in MoS_2 at wafer scale. We anticipate that the scalability and ease of implementation of this approach will open up avenues to develop wafer-scale 2D material circuitry hitherto unexplored.

2. PL Enhancement Indicates Dedoping of Large-Area Monolayer MoS_2 upon Illumination

Wafer-scale semiconducting 2H MoS_2 grown by CVD is used for this study (Figures S1 and S2, Supporting Information). Raman spectroscopy confirmed that the MoS_2 (**Figure 1a**, photograph) is monolayer (≈19 cm^{-1} separation between E_{2g} and A_{1g} modes) and in the 2H phase (Figure 1b). Raman mapping confirms the homogeneity of the film (Figure S3, Supporting Information), and high-angle annular dark field scanning transmission electron microscopy (HAADF-STEM, Figure 1c) confirms the 2H MoS_2 phase and film quality. HAADF-STEM images (Figure S4, Supporting Information) show presence of atomic defects in the as grown film. In addition, the A and B exciton absorption positions at 1.87 and 2.02 eV (Figure S5, Supporting Information) further confirms monolayer MoS_2.[30]

Interestingly, PL measurements on the MoS_2 films show changes in intensity and peak position upon illumination with a 532 nm laser under ambient conditions (Figure 1d). While the PL is initially weak due to the n-type doping as grown,[51,52] there is almost 80x enhancement upon illumination. The PL peak also blue shifts 10 meV for the initial 19 min before stabilizing (Figure 1d, sample 1). The absolute magnitudes of PL changes (both intensity and peak position) showed minor variations depending on the point measured; however, the trends in PL intensity and peak position (Figure 1e) were qualitatively similar for all points. For example, although a more sudden change in peak position is observed for point 2 at initial times possibly due to variations in defect densities, the general trends (PL intensity increase and blue shift) remained the same. The blue shift and increased intensity in MoS_2 PL can be explained by spectral redistribution as the dominant PL character changes from charged exciton (trion) to neutral exciton emission. These observations indicate a reduction in doping level upon illumination with 532 nm laser under ambient conditions. The integrated PL intensity for various illumination times is shown in Figure S6a (Supporting Information), where the PL changes show a saturation behavior and eventually plateau.

Significant PL enhancement was only seen for an illumination laser photon energy exceeding the MoS_2 bandgap (E_g = 1.87 eV; e.g., 532 nm (2.33 eV) and 633 nm (1.96 eV) lasers), while sub-bandgap illumination with 785 nm (1.58 eV) did not generate significant changes in PL (Figure S6b, Supporting Information). Note that the illumination laser wavelength varies for these measurements (532, 633, or 785 nm), but the PL measurement is always performed with 532 nm excitation laser light.

Raman modes are used to determine changes in carrier concentration and strain in monolayer MoS_2, where the A_{1g} mode is more sensitive to carrier concentration (doping) and the E_{2g} mode is more sensitive to strain.[52,53] Raman mapping confirmed differences in peak position for the illuminated and not illuminated regions of the MoS_2 for both the A_{1g} and E_{2g} modes

© 2024 The Author(s). Advanced Materials published by Wiley-VCH GmbH

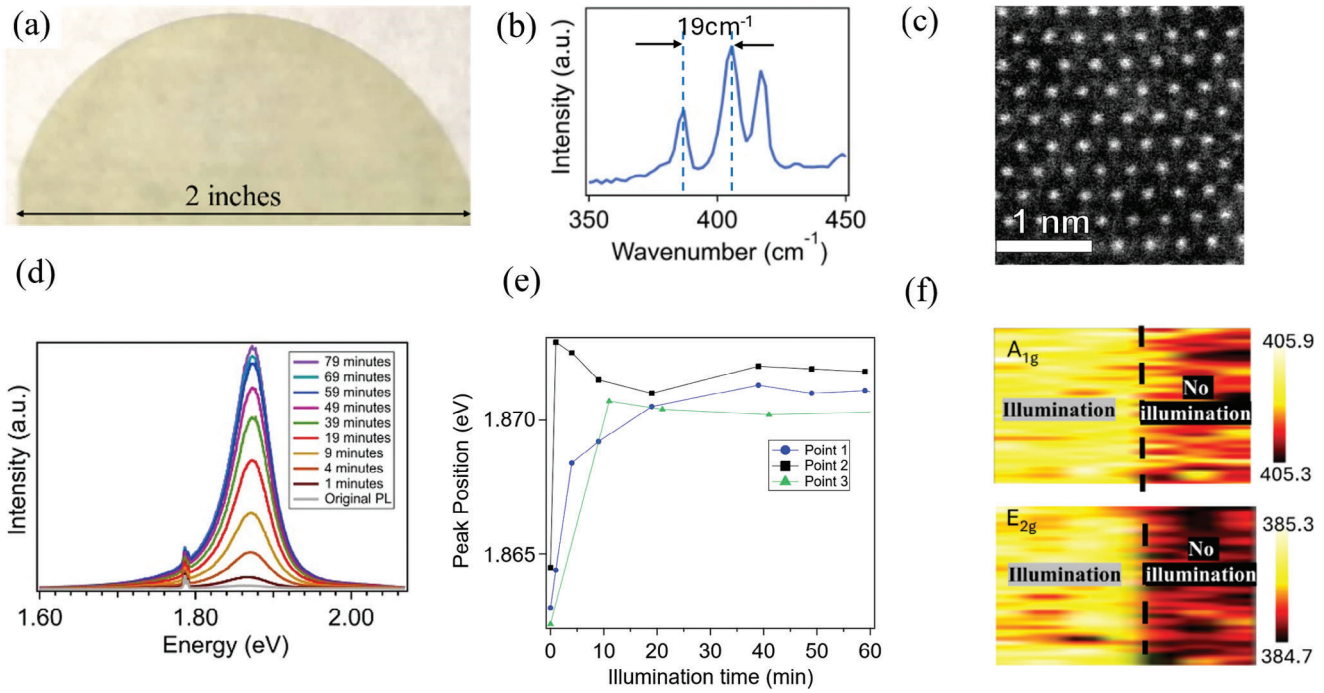

Figure 1. Photo-dedoping effect in monolayer MoS_2. a) Camera image of wafer scale MoS_2. b) Raman splitting confirming MoS_2 with splitting between the E_{2g} and A_{1g} modes of 19 cm^{-1}. c) HAADF-STEM image from monolayer MoS_2. d) Photosoaking effect in MoS_2 showing increase in PL upon illumination with 532 nm laser at a power density of 423.7 μW μm^{-2}. e) Changes in peak position of monolayer MoS_2 as a function of illumination time. f) Raman shift mapping data for the A_{1g} mode of MoS_2 (top panel) and E_{2g} mode (bottom panel) with/without 532 nm illumination. Units for both the color scales are cm^{-1}.

(Figure 1f). Illuminated areas resulted in the A_{1g} mode shifting to higher energy (Figure 1f) and a narrower FWHM (Figure S7, Supporting Information) consistent with dedoping of MoS_2. The change in E_{2g} mode (Figure 1f) suggests changes in strain on the MoS_2 lattice upon illumination (possibly due to surface modification).[52,53] Trends from the Raman shifts as well as PL enhancements insinuate (and are consistent with) dedoping upon illumination.

3. KPFM Confirms that PL Changes are Related to Photo-Dedoping

By rastering a focused laser beam using the confocal Raman/PL setup, we produced well controlled photo-patterns (details in the Experimental section) on the MoS_2 with high spatial fidelity that can be mapped with PL and Kelvin Probe Force Microscopy (KPFM) measurements to better understand the changes driving PL enhancements.

PL maps and corresponding surface potential images (measured on the same area) mirror each other, showing obvious anti-correlations between spatially dependent PL intensity and surface potential of the MoS_2 film (**Figure 2**c,d). The areas of MoS_2 illuminated with the 532 nm laser (green stripes in Figure 2a) showed a concomitant increase in PL (Figure 2c) and decrease in surface potential (Figure 2d,f), both of which are consistent with the initially n-type MoS_2 Fermi level moving toward the middle of the bandgap (becoming more intrinsic). Analysis of the KPFM images reveals a distribution of measurements with different potentials centered ≈170 and ≈230 mV for areas that were and were not exposed to illumination (Figure 2e). AFM topography line scans (Figure 2b) confirmed no significant topographic changes within the sensitivity limits of 0.5 nm.

However, zoomed in KPFM (Figure S8a, Supporting Information) and AFM topography (Figure S8b, Supporting Information) measurements on a cleaner part of the sample (with minimal particles) showed minor changes in topography on the illuminated parts. A line scan (along the blue line) shows no significant variation in topography (Figure S8c, Supporting Information) as discussed. However, averaging of all lines in the zoomed in section (Figure S8d, Supporting Information) leads to better signal to noise and enables visualization of very minor changes in topography at the same positions on the sample where the surface potential changes due to exposure (Figure S8e, Supporting Information). Interestingly, instead of seeing a dip in topography due to etching upon illumination (as reported at laser powers about an order of magnitude higher than used in this study),[35] we observe a slight increase of ≈2 Å in height/topography at the illuminated parts confirming no sample etching under the lower laser powers (used in this study). This is consistent with the change in E_{2g} mode (Figure 1f) suggesting changes in strain on the MoS_2 lattice upon illumination (possibly due to surface modification). Therefore, the increase in PL and work function can be directly attributed to photo-dedoping with the MoS_2 becoming more intrinsic (likely due to surface modification as discussed earlier) and the PL more excitonic in nature. The ability to change doping levels in monolayer MoS_2 upon illumination offers distinctive capabilities for spatial control over carrier densities by selectively exposing chosen regions to light.

© 2024 The Author(s). Advanced Materials published by Wiley-VCH GmbH

15214095, 2025, 3, Downloaded from https://advanced.onlinelibrary.wiley.com/doi/10.1002/adma.202409825 by National Renewable Energy Lab, Wiley Online Library on [24/01/2025]. See the Terms and Conditions (https://onlinelibrary.wiley.com/terms-and-conditions) on Wiley Online Library for rules of use; OA articles are governed by the applicable Creative Commons License

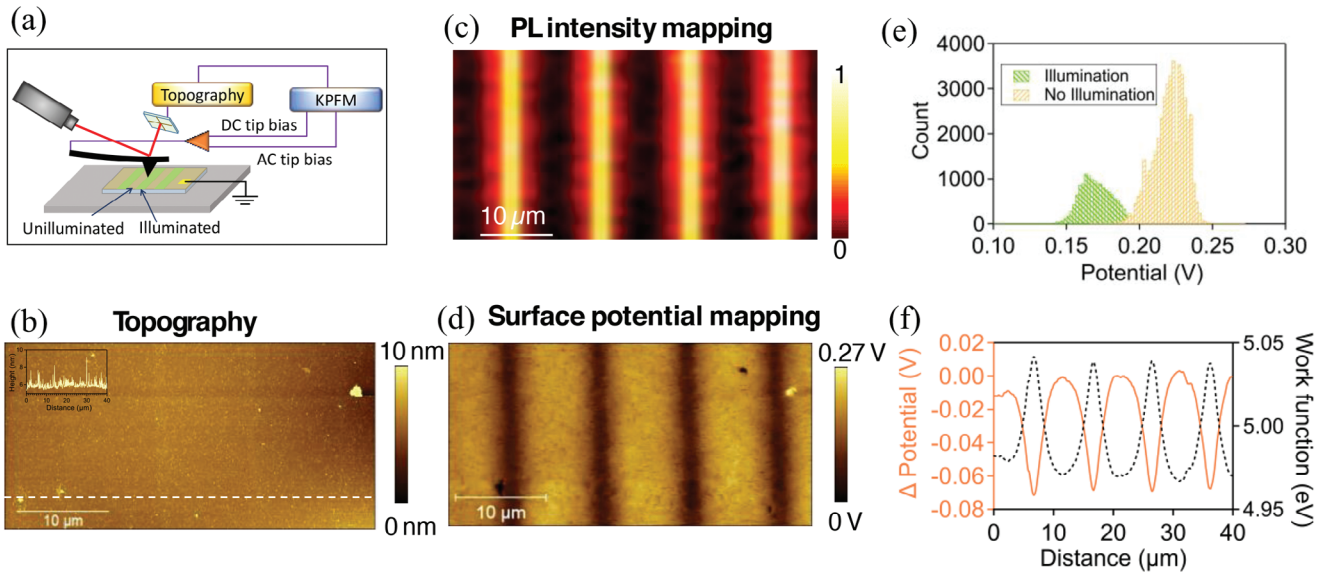

Figure 2. KPFM measurements for confirmation of photo-dedoping upon illumination. a) Schematic of the KPFM setup for mapping changes in surface potential between the illuminated and not illuminated parts. b) AFM images show no significant changes in the topography of the areas with and without illumination. c) PL mapping data showing increments in PL at 1.87 eV upon illumination. PL intensity has been normalized to the pixel with the highest intensity. d) KPFM data is anti-correlated with the PL, illustrating decreased surface potential with increased PL. e) Distribution of surface potential for illuminated and not illuminated parts. f) Variation of surface potential and work function as a function of position.

4. Fine Control of Doping Density with Illumination Time

We further investigated the role of the illumination conditions to elicit better control over photo-dedoping in large area monolayer MoS_2. KPFM (**Figure** 3a) and PL (Figure 3b) mapping show changes in surface potential and emission intensity with different illumination times between 1 and 30 s at fixed power density. Longer illumination times produce larger shifts in surface potential and more intense PL emission. The illumination time dependence of surface potential and PL are strongly correlated, as shown in the line scans of Figure 3c,d, respectively.

Although the power density for all illumination times in Figure 3a,b is identical, the area affected by illumination changes

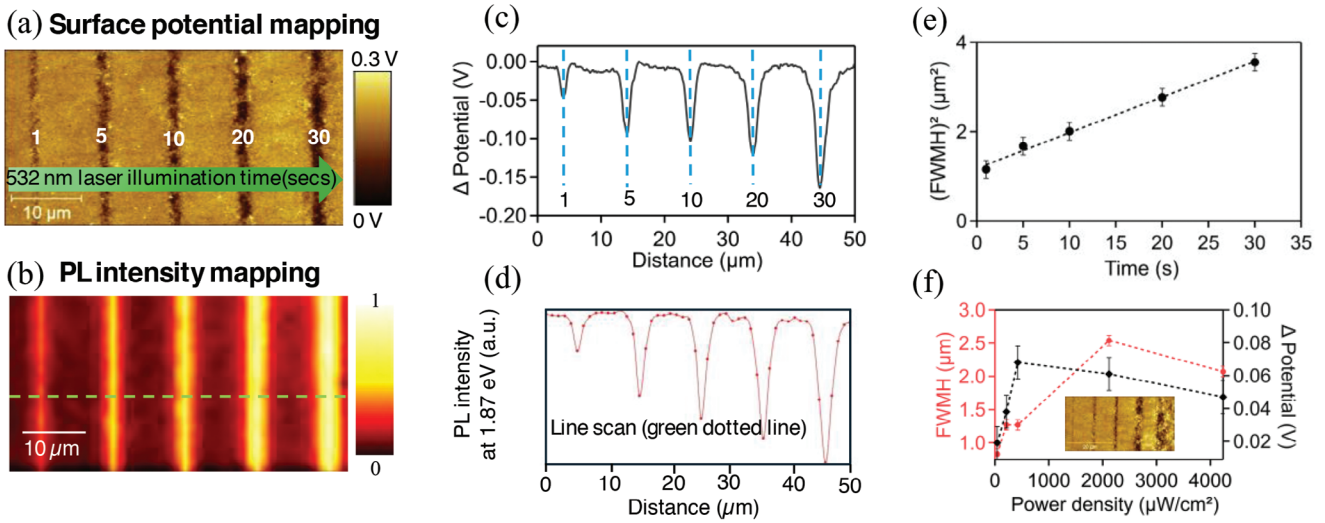

Figure 3. Influence of illumination conditions, i.e., time and power on photo-dedoping process. a–e) shows data for various laser illumination times ranging from 1 to 30 s where the laser power is 423.7 μW μm^{-2}. (f) shows data for different laser power densities. a) KPFM data showing changes in potential as the illumination time is varied. The numbers in white represent illumination time in seconds. b) Corresponding PL mapping data showing PL with increase in illumination time. The mapping data were acquired at 1.87 eV emission energy, and PL intensity has been normalized to the pixel with the highest intensity. c) Average line scan for potential changes extracted from the KPFM data. The average is taken along the y-direction in panel (a). d) Line scan of PL at 1.87 eV along the green dash line in panel (b). e) Change in $(FWHM)^2$ for potential peaks signifying broadening due to diffusion. f) Influence of power density of illumination on photo-dedoping process.

© 2024 The Author(s). Advanced Materials published by Wiley-VCH GmbH

15214095, 2025, 3, Downloaded from https://advanced.onlinelibrary.wiley.com/doi/10.1002/adma.202409825 by National Renewable Energy Lab, Wiley Online Library on [24/01/2025]. See the Terms and Conditions (https://onlinelibrary.wiley.com/terms-and-conditions) on Wiley Online Library for rules of use; OA articles are governed by the applicable Creative Commons License

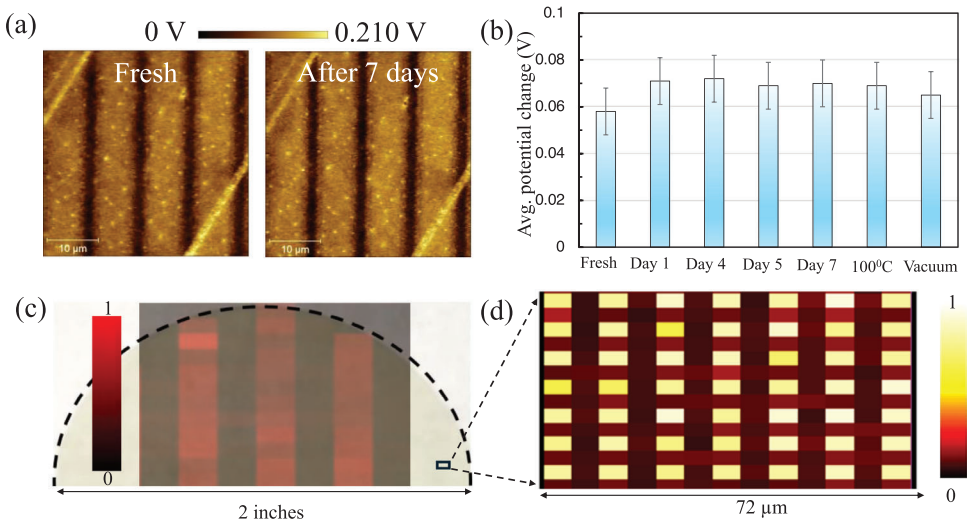

Figure 4. Evaluating performance of the photo-dedoping process. a) KPFM images comparing changes in photo-dedoping with high spatial resolution immediately after illumination and after 7 days post illumination. b) Comparisons of change in potential (between the laser illuminated and not illuminated parts) over various stressing conditions like time, temperature, and vacuum. c) Photo-dedoping at wafer scale showing scalability of the process. PL intensity at 1.87 eV has been normalized to the pixel with the highest intensity. d) Photo-dedoping at a much smaller length scale showing control over spatial resolution of photo-dedoping with high spatial fidelity. PL intensity at 1.87 eV has been normalized to the pixel with the highest intensity.

(Figure 3e). The broadening at the same power densities for different illumination times implicates additional mechanism(s) beyond light scattering. This broadening could arise from excitons or free carriers diffusing out of the illuminated area, leading to changes in dedoping densities over larger areas compared to the laser beam (≈1.5 μm) itself. As soon as the immediate area in the laser spot has been dedoped, carriers and excitons could diffuse beyond the illuminated area as their lifetime in the illuminated area increases and so they progressively reach further outward. To confirm this, we fit the full width half maximum (FWHM), of each peak in the Δ Potential scan of Figure 3c to the diffusion equation (FWHM-FWHM(t = 0)$\propto$(Dt)$^{1/2}$) (Figure 3e) and found good agreement. The FWHM at t = 0 is 1.08 μm, in good agreement with the known beam size. The fitting results in a diffusion coefficient of 0.03 μm^2 s^{-1}, which is ≈5 orders of magnitude slower than expected from the electron diffusion coefficient (10 cm^{2}V^{-1}s^{-1}).[54] Thus, the diffusion behavior is limited by the kinetics of the dedoping process and not carrier transport. Ultimately this means that the best possible lateral resolution of the dedoping process is limited by the beam profile. Figure 3f shows the influence of laser power on the dedoping process. At low power intensity, the PL intensity/degree of dedoping scales linearly with illumination power. However, higher powers (2.1 and 4.2 mW μm^{-2}) result in sample degradation.

5. Stability and Scalability of Photo-Dedoping

The stability of dopants under ambient conditions as well as processing conditions form an important metric for device integration and performance.[13] **Figure** 4a shows comparison for the surface potential maps of a freshly photo-dedoped sample (few hours after exposure/illumination) and sample left in ambient conditions post photo-dedoping up to 7 days. It can be seen that there is hardly any change in the local doping densities of the samples for a period of 7 days signifying exceptional stability of the photo-dedoping procedure under ambient conditions. KPFM images during intermediate periods (after 4 and 5 days) are shown in Figure S9a,b (Supporting Information).

To further understand the stability, we subject the 7-day old photo-dedoped MoS_2 films to temperature (100 °C for 30 min, Figure S9c, Supporting Information) and vacuum (10 mTorr, Figure S9d, Supporting Information) treatments. These additional stress tests demonstrate the resilience of the photo-dedoping process to technologically relevant device processing conditions. Figure 4b summarizes the average surface potential difference between the illuminated (dedoped) and not illuminated (as grown) parts as a function of these various processing/stressing conditions. There is a small increase in the surface potential change between the "fresh" dedoped measurement and the other measurements at later times and with temperature and vacuum treatments. This small variation is within the error of the measurement, however, is likely real and due to the presence of transient effects (pre-equilibrium) from long-lived carriers (discussed in later section). We also tried testing the stability of the dedoping by PL measurements (Figure S10, Supporting Information), but the illumination with the laser excitation resulted in slight dedoping during the PL data acquisition, demonstrating the utility of KPFM for such stability measurements of photosensitive samples.

We also demonstrate the remarkable scalability and precision of photo-dedoping in MoS_2, enabling patterning over very large areas while maintaining fine spatial control. Specifically, we patterned across a 2-inch wafer (Figure 4c) to showcase scalability. Simultaneously, we demonstrated significantly higher spatial fidelity on the same wafer (Figure 4d), highlighting the precision of our technique. The high-spatial dedoping that can be achieved is constrained by the laser spot size and diffusion limits (1–2 μm) as discussed earlier.

© 2024 The Author(s). Advanced Materials published by Wiley-VCH GmbH

15214095, 2025, 3, Downloaded from https://advanced.onlinelibrary.wiley.com/doi/10.1002/adma.202409825 by National Renewable Energy Lab, Wiley Online Library on [24/01/2025]. See the Terms and Conditions (https://onlinelibrary.wiley.com/terms-and-conditions) on Wiley Online Library for rules of use; OA articles are governed by the applicable Creative Commons License

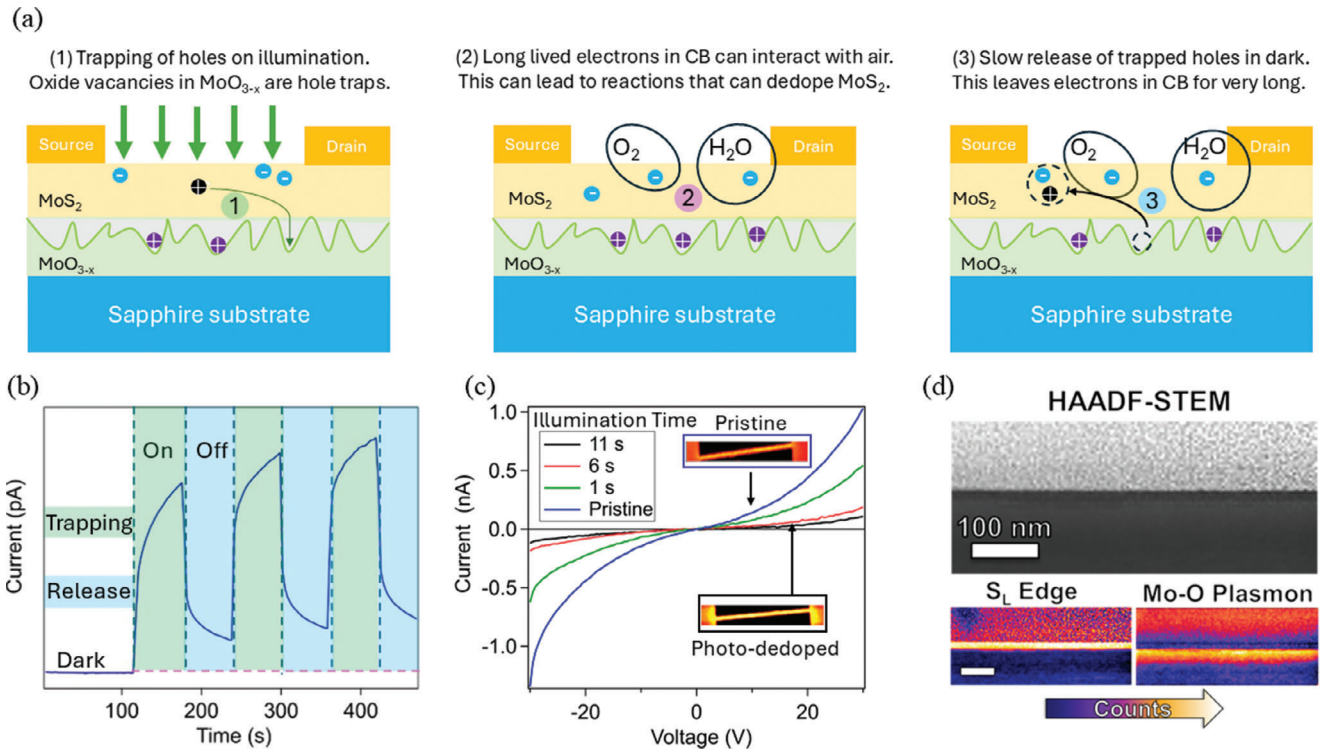

Figure 5. Mechanism for photo-dedoping and change in channel conductance. a) Mechanism for dedoping upon illumination. Step i): The photoexcited holes get trapped in the MoO_{3-x} layer. This leads to a gradual increase in conductivity of the channel after the initial increase upon illumination due to photogating effect. Step ii): The long-lived excited state electrons are energetic enough to participate in photoreactions in the presence of ambient air. This possibly leads to passivation of S vacancies (defects) on MoS_2. Concomitantly, this leads to the photo-dedoping effect. Step iii): The holes are gradually released from the trapping layer when the light is turned off. This results in a slow decay in channel current after the initial decrease. b) Transient measurements provide insights into the trapping/detrapping process upon illumination/dark. This complements the mechanism for photo-dedoping in Figure 5a. c) *I–V* sweeps showing change in channel conductance post photo-dedoping. Inset shows the PL of the original sample and PL after 11 s illumination leading to photo-dedoping. The brighter regions (red/yellow) correspond to PL signal from MoS_2 and the darker (black) regions correspond to areas on the gold pad where there is no MoS_2 PL signal. Post dedoping the PL signal from the MoS_2 gets stronger. d) STEM/EELS confirming the presence of the MoO_{3-x} layer. This oxide layer likely plays a critical role in trapping holes, enabling long-lived electrons in the conduction band in the dark.

6. Mechanism for Photo-Dedoping and Impact on Conductivity

Two-terminal devices with channel widths of 10 µm were fabricated for electrical transport measurements (Figure S11, Supporting Information). The device fabrication process is discussed in detail in the material and methods section. **Figure** 5a highlights the critical steps during the dedoping process that are elucidated by electrical measurements in Figure 5b,c. Upon illumination, excitons are formed in MoS_2, which dissociate into electron hole pairs on the application of electrical bias between the source and the drain leading to an increase in channel conductance with a fast and slow component (Figure 5b, green shaded region). The fast component is attributed to immediate excess free carrier generation upon illumination, while the slow component is attributed to a photogating effect (Figure 5a, part 1). The photogating effect has been observed in MoS_2 on amorphous oxide surfaces with oxygen vacancies, which act as trap sites for holes.[55–57]

To investigate the oxide layer, we used X-ray photoelectron spectroscopy (XPS), STEM-EELS, and Confocal Raman spectroscopy. The XPS data (Figure S12, Supporting Information) suggests the presence of MoO_3 like layer, while HAADF-STEM (top panel Figure 5d) spatially resolves an oxide buffer layer between the MoS_2 and sapphire. The oxygen K-edge fine structure from STEM-EELS displayed a peak for the crystalline oxide in the sapphire substrate (≈530 eV), which is not observed in the amorphous oxide layer directly underneath the deposited MoS_2 sample, indicating the oxide buffer layer is amorphous (Figure S13, Supporting Information). Furthermore, the absence of signature MoO_3 Raman peaks confirms the amorphous nature. Together, the XPS, HAADF-STEM and Raman, allow us to assign the oxide underneath MoS_2 film as amorphous sub-stoichiometric MoO_{3-x}. The MoO_{3-x} hole trapping layer plays a critical role in photo-dedoping MoS_2 in the presence of oxygen and moisture in ambient air. Hole trapping leads to the longer lifetime of electrons in the conduction band (CB) (during/post illumination). These electrons can participate in reactions with H_2O and O_2, likely leading to passivation of sulfur vacancies (defects) and dedoping of MoS_2 (Figure 5a, part 2). We observe the long-lived electrons as a slow decrease in the measured MoS_2 photocurrent after stopping illumination, as the holes are slowly detrapped from the oxide layer and recombine with the electrons (Figure 5a, part 3 and Figure 5b, blue shaded region). While the photoconductivity

© 2024 The Author(s). Advanced Materials published by Wiley-VCH GmbH

15214095, 2025, 3, Downloaded from https://advanced.onlinelibrary.wiley.com/doi/10.1002/adma.202409825 by National Renewable Energy Lab, Wiley Online Library on [24/01/2025]. See the Terms and Conditions (https://onlinelibrary.wiley.com/terms-and-conditions) on Wiley Online Library for rules of use; OA articles are governed by the applicable Creative Commons License

decay is extremely slow (takes hours to reach steady state), the reaction of excited electrons with ambient air (O_2 and/or H_2O) dedoping the MoS_2 occurs at much shorter timescales as measured by PL and KPFM. The long-lived electrons in the CB yield higher conductivity of the illuminated samples immediately after exposure leading to results that can be perceived as contradictory to our dedoping claims. Therefore, we measured the temporal dependence of current post-illumination and found that it takes ≈65 min for the dark current to fall below the dark current of the original (as grown) sample and even longer to reach steady state (≈ 4–5 h) (Figure S14, Supporting Information). We evaluated how photo-dedoping in MoS_2 measured with PL translated to changes in dark conductivity at steady state (measured after a day to ensure steady state, Figure S15, Supporting Information). As expected, different illumination times lead to different channel conductivities. We see almost an order of magnitude decrease with respect to as grown MoS_2 in steady-state dark current with an illumination time of 11 s (Figure 5d). Corresponding PL images are shown in the inset and agree with our conclusions that the samples are dedoped with illumination. Our proposed mechanism highlights the critical roles of both ambient air and the oxide interface in the dedoping process.

In order to get more insights into the mechanism for dedoping under illumination and ascertain the critical role of the oxide interface as well as moisture/O_2, we performed several control experiments. First, we did PL measurements of MoS_2 monolayers i) with the oxide interfacial layer resulting from CVD growth in an air-free cell (N_2 environment to eliminate H_2O/O_2) and ii) transferred to other substrates where the oxide interfacial layer is removed/changed due to transfer from growth substrate. PL measurements in the air-free cell and on the transferred samples (on SiO_2/Si or fresh sapphire) showed no significant photo-dedoping, highlighting the critical role of both ambient conditions and buffer oxide interfaces, respectively, in the dedoping process (Figure S16, Supporting Information). Second, IV measurements (in dark) (Figure S17a, Supporting Information) were performed on as-grown MoS_2 samples containing the oxide interfacial layer. Here the samples were illuminated in an air-free cell and then kept in the air-free cell for a day to allow detrapping of the holes and a return to equilibrium before taking out to ambient air for IV measurements. This device showed no significant change in channel conductance before and after illumination again confirming the role of ambient air exposure for photo-dedoping MoS_2. Interestingly, samples that were illuminated in an air-free cell and taken out immediately into ambient conditions did show photo-dedoping (Figure S17b, Supporting Information), again confirming the critical and necessary role of long-lived carriers in the dedoping process.

7. Conclusion

In this work, we unravel the mechanism that drives PL changes of MoS_2 monolayers under laser illumination in ambient conditions. We demonstrate the critical role of the hole trap states within the oxide interface between the MoS_2 and the substrate for driving stable and long lived dedoping in wafer scale monolayer MoS_2. We propose that the oxide layer captures photoexcited holes, allowing long-lived electrons to remain available for surface reactions at sulfur vacancies (defect sites) in ambient air, ultimately leading to dedoping. KPFM measurements confirm changes in fermi level position upon laser illumination leading to localized dedoping of monolayer MoS_2. We leverage this understanding to develop a scalable process with excellent spatial resolution to change doping densities in wafer scale monolayer MoS_2 by either controlling the illumination time or the power density. Further, time-lapsed KPFM measurements confirm that this dedoping is very stable under ambient conditions (at least 7 days) and survives high temperatures and vacuum conditions making it feasible for commercial deployment in semiconductor fabrication. We anticipate this ability to photo-dedope MoS_2 can be extended to other TMDCs where similar enhancements in PL upon illumination have been observed, in addition, the photo-dedoping should be achieved with any light source, such as a light emitting diode, provided the photon energy is greater than the bandgap. This demonstration opens up unique possibilities for wafer scale, multi-logic devices with 2D atomically thin TMDCs for next generation electronic and optoelectronic devices.

8. Experimental Section

Synthesis of Large Area Monolayer MoS_2 Films: MoS_2 is grown in a 3-zone tube furnace by CVD. Solid phase precursors (MoO_3 and S) are loaded in separate heating zones of the CVD furnace and heated at different temperatures. The substrate (sapphire) is placed downstream in another zone that is maintained at a separate temperature. The schematic for the furnace and the temperature profiles are shown in Figure S1 (Supporting Information). Argon is used as a carrier gas. The substrates are annealed before growth for high quality MoS_2 growth. During the anneal and growth, the pressure is maintained at 2 Torr. The substrates are annealed at 990 °C with flow rate of Ar maintained at 274 sccm and O_2 maintained at 5.56 sccm for 1.5 h. The growth starts 25 min after the completion of annealing. The flow rate of Ar during the growth is maintained at 150 sccm. The substrates are placed in the heating zone of the furnace, which is maintained at 900 °C, the MoO_3 is maintained at 530 °C. The S is heated with an external heating belt maintained at 150 °C.

Photo-Patterning Procedure: High spatial fidelity photo-patterns were produced on MoS_2 by scanning the laser spot with local illumination at each one-micron spot for 30 s. This resulted in lines with illumination time of ≈30 s. Multiple lines were created by rastering the laser. The spatial separation between 2 illuminated lines was maintained at 10 µm unless otherwise specified.

PL and Raman Measurements: PL and Raman measurements were performed using the Renishaw inVia confocal system by using the 532 nm laser line and the 50x long working distance (50 mm) objective lens (spot size 1.5 µm diameter). The PL measurements were done at a laser power of 1% (total power 75 µW) unless otherwise specified. Wavelength dependent measurements were done at laser power of 1% (of total power) for all the lasers. The scattering light from the sample was directed by a grating with 1800 lines mm^{-1} for Raman or 600 lines mm^{-1} for PL prior to the CCD detector. The typical exposure time is 1 s with two accumulations for PL measurements.

KPFM Measurements: KPFM is an extension of the AFM technique. In KPFM, a conductive probe is used to record the surface potential of the sample, which is related to the work function of the sample surface. For semiconductors, the work function is defined as the energy difference between the Fermi energy level and the vacuum level. Thus, the surface potential obtained through KPFM is also related to the Fermi energy of the sample surface. Here, the surface potential images of the samples were obtained using the homemade KPFM with ≈30 nm spatial and ≈10 mV voltage resolutions. A Pt/Ir-coated conductive silicon AFM probe (Nanosensor PPP-EFM) with a tip apex radius of < 25 nm was used. For KPFM surface potential imaging, the second harmonic resonant oscillation frequency of the probe cantilever at 300–400 kHz was used, whereas the first harmonic resonance frequency at ≈60 kHz was utilized for AFM

© 2024 The Author(s). Advanced Materials published by Wiley-VCH GmbH

15214095, 2025, 3, Downloaded from https://advanced.onlinelibrary.wiley.com/doi/10.1002/adma.202409825 by National Renewable Energy Lab, Wiley Online Library on [24/01/2025]. See the Terms and Conditions (https://onlinelibrary.wiley.com/terms-and-conditions) on Wiley Online Library for rules of use; OA articles are governed by the applicable Creative Commons License

topography imaging. A gold contact was deposited on the sample to ground the sample during KPFM measurement. The measured surface potential (also known as contact potential difference, V_{CPD}) is defined as:

$$V_{CPD} = \left(\Phi_{tip} - \Phi_{sample}\right)/e \quad (1)$$

where Φ_{sample} and Φ_{tip} are work functions of the sample and the tip respectively. Freshly exfoliated highly oriented pyrolytic graphite (HOPG), having a known work function of 4.60 eV, was used as a reference to estimate the work function of the tip (Figure S18, Supporting Information). The measured V_{CPD} between tip and HOPG was 0.60 ± 0.01 eV, from which it is estimated that Φ_{tip} was 5.10 ± 0.01 eV. This work function value of the probe is used to obtain the change in work function of the monolayer MoS_2 upon illumination.

Device Fabrication: Source (S) and Drain (D) pads were laid on the monolayer MoS_2 by standard photo lithography and metallization technique in the clean room. Initially S1818 positive photo resist was spin coated on top of substrate/MoS_2 at 4000 RPM for 30 s followed by baking at 100 °C on the hot plate. The photoresist coated substrates were exposed to UV light of wavelength $\lambda = 386$ nm for 5.2 s through the photomask with the help of mask aligner. This was followed by developing the photo resist in MF351: DI = 1:5 developer for 60 s and rinsing in DI water. Finally, to complete the device fabrication process, a metallization process using an e-beam evaporator was employed. Ti/Au = 5/50 nm was deposited at 10^{-6} Torr. The lift-off procedure was performed in acetone for 15 min followed by rinsing in IPA and drying in N_2 to attain S and D terminals. The quality of developing and lift-off was confirmed by microscope.

Transport Measurements: Two-terminal current–voltage (I–V) characteristics of a planar MoS_2 device were carried out between source and drain terminals by utilizing the SMU unit of Keithley 4200-SCS parameter analyzer. All electrical measurements were conducted inside the probe station in dark at ambient atmosphere and pressure unless specified otherwise. Electrical contacts with the source and drain pads were made using spring-loaded micromanipulators with the aid of an optical microscope. The devices were allowed to rest for several hours before recording the actual I-V measurements, ensuring the system returned to equilibrium and reached steady-state conditions. This process helped eliminate any transient effects caused by illumination during sample examination under the microscope. After a sufficient resting period, I–V curves were recorded by sweeping the voltage form −30 to 30 V in step of 0.5 V and the corresponding current was collected. The transient data (current as a function of time) were recorded by biasing the voltage at 20 V.

TEM Measurements: All TEM data were acquired using a Nion UltraSTEM 100 equipped with a Dectris ELA direct electron detector. The accelerating voltage of the electrons were set to 60 kV, a convergence semiangle of 30 mrad, and an EELS collection semi-angle of ≈48 mrad. A 2 mm EELS aperture was used to maximize the signal from the core-loss spectrum images.

XPS Measurements: XPS data were obtained on a Physical Electronics Versa Probe III using Al Kα radiation. The XPS setup was calibrated with Au and/or Cu metal, which was cleaned via Ar-ion sputtering. The raw atomic concentration has a 5% error due to small signal to noise ratios of the monolayer and literature sensitivity values for peak integration. For these MoS_2 measurements on sapphire, the neutralizer was used (Ar ions and electrons) to compensate for charging effect.

Supporting Information

Supporting Information is available from the Wiley Online Library or from the author.

Acknowledgements

This work was authored in part by the National Renewable Energy Laboratory, operated by Alliance for Sustainable Energy, LLC, for the U.S. Department of Energy (DOE) under Contract No. DE-AC36-08GO28308. Funding provided by Solar Photochemistry Program, Division of Chemical Sciences, Geosciences, and Biosciences, Office of Basic Energy Sciences, U.S. Department of Energy. The development and application of the modified probe station to allow in situ device transport measurements of the photo-dedoping process was performed at the National Renewable Energy Laboratory and supported by the Reconfigurable Materials Inspired by Nonlinear Neuron Dynamics (reMIND) Energy Frontier Research Center funded by the U.S. Department of Energy (DOE), Office of Science, Office of Basic Energy Sciences. C.S. received support from the U.S. DOE, Office of Science, Office of Workforce Development for Teachers and Scientists (WDTS) under the Science Undergraduate Laboratory Internships (SULI) Program. L.H. received support from Graduate Assistantship in Areas of National Need (GAANN) fellowship in Quantum Engineering. K.B. time was supported by the Virginia space grant consortium program under award number 005604. A portion of this research was conducted at the Center for Nanophase Materials Sciences, which is a DOE Office of Science User Facility.

Conflict of Interest

The authors declare no conflict of interest.

Data Availability Statement

The data that support the findings of this study are available from the corresponding author upon reasonable request.

Keywords

2D materials, optoelectronics, photo-dedoping, wafer-scale manipulation

Received: July 8, 2024
Revised: October 9, 2024
Published online: October 23, 2024

[1] A. Splendiani, L. Sun, Y. Zhang, T. Li, J. Kim, C.-Y. Chim, G. Galli, F. Wang, *Nano Lett.* **2010**, *10*, 1271.
[2] K. F. Mak, C. Lee, J. Hone, J. Shan, T. F. Heinz, *Phys. Rev. Lett.* **2010**, *105*, 136805.
[3] V. K. Sangwan, M. C. Hersam, *Nat. Nanotechnol.* **2020**, *15*, 517.
[4] N. Li, Q. Wang, C. Shen, Z. Wei, H. Yu, J. Zhao, X. Lu, G. Wang, C. He, L. Xie, J. Zhu, L. Du, R. Yang, D. Shi, G. Zhang, *Nat. Electron.* **2020**, *3*, 711.
[5] T. Li, W. Guo, L. Ma, W. Li, Z. Yu, Z. Han, S. Gao, L. Liu, D. Fan, Z. Wang, Y. Yang, W. Lin, Z. Luo, X. Chen, N. Dai, X. Tu, D. Pan, Y. Yao, P. Wang, Y. Nie, J. Wang, Y. Shi, X. Wang, *Nat. Nanotechnol.* **2021**, *16*, 1201.
[6] Y. Xia, X. Chen, J. Wei, S. Wang, S. Chen, S. Wu, M. Ji, Z. Sun, Z. Xu, W. Bao, P. Zhou, *Nat. Mater.* **2023**, *22*, 1324.
[7] L. Li, Q. Wang, F. Wu, Q. Xu, J. Tian, Z. Huang, Q. Wang, X. Zhao, Q. Zhang, Q. Fan, X. Li, Y. Peng, Y. Zhang, K. Ji, A. Zhi, H. Sun, M. Zhu, J. Zhu, N. Lu, Y. Lu, S. Wang, X. Bai, Y. Xu, W. Yang, N. Li, D. Shi, L. Xian, K. Liu, L. Du, G. Zhang, *Nat. Commun.* **2024**, *15*, 1825.
[8] M. Chubarov, T. H. Choudhury, D. R. Hickey, S. Bachu, T. Zhang, A. Sebastian, A. Bansal, H. Zhu, N. Trainor, S. Das, M. Terrones, N. Alem, J. M. Redwing, *ACS Nano* **2021**, *15*, 2532.
[9] J. Kwon, M. Seol, J. Yoo, H. Ryu, D.-S. Ko, M.-H. Lee, E. K. Lee, M. S. Yoo, G.-H. Lee, H.-J. Shin, J. Kim, K.-E. Byun, *Nat. Electron.* **2024**, *7*, 356.

© 2024 The Author(s). Advanced Materials published by Wiley-VCH GmbH

15214095, 2025, 3, Downloaded from https://advanced.onlinelibrary.wiley.com/doi/10.1002/adma.202409825 by National Renewable Energy Lab, Wiley Online Library on [24/01/2025]. See the Terms and Conditions (https://onlinelibrary.wiley.com/terms-and-conditions) on Wiley Online Library for rules of use; OA articles are governed by the applicable Creative Commons License

[10] J.-H. Fu, J. Min, C.-K. Chang, C.-C. Tseng, Q. Wang, H. Sugisaki, C. Li, Y.-M. Chang, I. Alnami, W.-R. Syong, C. Lin, F. Fang, L. Zhao, T.-H. Lo, C.-S. Lai, W.-S. Chiu, Z.-S. Jian, W.-H. Chang, Y.-J. Lu, K. Shih, L.-J. Li, Y. Wan, Y. Shi, V. Tung, *Nat. Nanotechnol.* **2023**, *18*, 1289.
[11] S. Das, A. Sebastian, E. Pop, C. J. McClellan, A. D. Franklin, T. Grasser, T. Knobloch, Y. Illarionov, A. V. Penumatcha, J. Appenzeller, Z. Chen, W. Zhu, I. Asselberghs, L.-J. Li, U. E. Avci, N. Bhat, T. D. Anthopoulos, R. Singh, *Nat. Electron.* **2021**, *4*, 786.
[12] D. Fan, W. Li, H. Qiu, Y. Xu, S. Gao, L. Liu, T. Li, F. Huang, Y. Mao, W. Zhou, W. Meng, M. Liu, X. Tu, P. Wang, Z. Yu, Y. Shi, X. Wang, *Nat. Electron.* **2023**, *6*, 879.
[13] J. Kim, M. Jung, D. U. Lim, D. Rhee, S. H. Jung, H. K. Cho, H.-K. Kim, J. H. Cho, J. Kang, *Nano Lett.* **2022**, *22*, 570.
[14] R. Younas, G. Zhou, C. L. Hinkle, *Appl. Phys. Lett.* **2023**, *122*, 160504.
[15] V. P. Pham, G. Y. Yeom, *Adv. Mater.* **2016**, *28*, 9024.
[16] W. Liu, J. Shi, L. Zhang, A. Han, S. Huang, X. Li, J. Peng, Y. Yang, Y. Gao, J. Yu, K. Jiang, X. Yang, Z. Li, W. Zhao, J. Du, X. Song, J. Yin, J. Wang, Y. Yu, Q. Shi, Z. Ma, H. Zhang, J. Ling, L. Xu, J. Kang, F. Xu, J. Liu, H. Liu, Y. Xie, F. Meng, et al., *Nat. Energy* **2022**, *7*, 427.
[17] *Nat. Electron.* **2021**, *4*, 699.
[18] Z. Li, T. Wang, Z. Lu, C. Jin, Y. Chen, Y. Meng, Z. Lian, T. Taniguchi, K. Watanabe, S. Zhang, D. Smirnov, S.-F. Shi, *Nat. Commun.* **2018**, *9*, 3719.
[19] C. Liu, H. Chen, X. Hou, H. Zhang, J. Han, Y.-G. Jiang, X. Zeng, D. W. Zhang, P. Zhou, *Nat. Nanotechnol.* **2019**, *14*, 662.
[20] Z. Zhao, S. Rakheja, W. Zhu, *Nano Lett.* **2021**, *21*, 9318.
[21] L. Ju, J. Velasco, E. Huang, S. Kahn, C. Nosiglia, H.-Z. Tsai, W. Yang, T. Taniguchi, K. Watanabe, Y. Zhang, G. Zhang, M. Crommie, A. Zettl, F. Wang, *Nat. Nanotech* **2014**, *9*, 348.
[22] M. S. Choi, A. Nipane, B. S. Y. Kim, M. E. Ziffer, I. Datta, A. Borah, Y. Jung, B. Kim, D. Rhodes, A. Jindal, Z. A. Lamport, M. Lee, A. Zangiabadi, M. N. Nair, T. Taniguchi, K. Watanabe, I. Kymissis, A. N. Pasupathy, M. Lipson, X. Zhu, W. J. Yoo, J. Hone, J. T. Teherani, *Nat. Electron.* **2021**, *4*, 731.
[23] F.-S. Yang, M. Li, M.-P. Lee, I.-Y. Ho, J.-Y. Chen, H. Ling, Y. Li, J.-K. Chang, S.-H. Yang, Y.-M. Chang, K.-C. Lee, Y.-C. Chou, C.-H. Ho, W. Li, C.-H. Lien, Y.-F. Lin, *Nat. Commun.* **2020**, *11*, 2972.
[24] S.-Y. Seo, G. Moon, O. F. N. Okello, M. Y. Park, C. Han, S. Cha, H. Choi, H. W. Yeom, S.-Y. Choi, J. Park, M.-H. Jo, *Nat. Electron.* **2020**, *4*, 38.
[25] E. Wu, Y. Xie, J. Zhang, H. Zhang, X. Hu, J. Liu, C. Zhou, D. Zhang, *Sci. Adv.* **2019**, *5*, eaav3430.
[26] R. Peng, Y. Wu, B. Wang, R. Shi, L. Xu, T. Pan, J. Guo, B. Zhao, C. Song, Z. Fan, C. Wang, P. Zhou, S. Fan, K. Liu, *Nat. Electron.* **2023**, *6*, 852.
[27] H. Kim, D.-H. Lien, M. Amani, J. W. Ager, A. Javey, *ACS Nano* **2017**, *11*, 5179.
[28] W. Shi, S. Kahn, L. Jiang, S.-Y. Wang, H.-Z. Tsai, D. Wong, T. Taniguchi, K. Watanabe, F. Wang, M. F. Crommie, A. Zettl, *Nat. Electron.* **2020**, *3*, 99.
[29] S.-J. Lee, Z. Lin, X. Duan, Y. Huang, *Nat. Electron.* **2020**, *3*, 77.
[30] M. Li, J. Yao, X. Wu, S. Zhang, B. Xing, X. Niu, X. Yan, Y. Yu, Y. Liu, Y. Wang, *ACS Appl. Mater. Interfaces* **2020**, *12*, 6276.
[31] D. Ghoshal, R. Kumar, N. Koratkar, *Inorg. Chem. Commun.* **2021**, *123*, 108329.
[32] J. Gao, Y. D. Kim, L. Liang, J. C. Idrobo, P. Chow, J. Tan, B. Li, L. Li, B. G. Sumpter, T. Lu, V. Meunier, J. Hone, N. Koratkar, *Adv. Mater.* **2016**, *28*, 9735.
[33] S. Y. Lee, U. J. Kim, J. Chung, H. Nam, H. Y. Jeong, G. H. Han, H. Kim, H. M. Oh, H. Lee, H. Kim, Y.-G. Roh, J. Kim, S. W. Hwang, Y. Park, Y. H. Lee, *ACS Nano* **2016**, *10*, 6100.
[34] J.-H. Ahn, W. M. Parkin, C. H. Naylor, A. T. C. Johnson, M. Drndić, *Sci. Rep.* **2017**, *7*, 4075.
[35] A. Castellanos-Gomez, M. Barkelid, A. M. Goossens, V. E. Calado, H. S. J. Van Der Zant, G. A. Steele, *Nano Lett.* **2012**, *12*, 3187.
[36] E. Kim, C. Ko, K. Kim, Y. Chen, J. Suh, S. Ryu, K. Wu, X. Meng, A. Suslu, S. Tongay, J. Wu, C. P. Grigoropoulos, *Adv. Mater.* **2016**, *28*, 341.
[37] T. H. Ly, Q. Deng, M. H. Doan, L.-J. Li, J. Zhao, *ACS Appl. Mater. Interfaces* **2018**, *10*, 29893.
[38] T. Afaneh, P. K. Sahoo, I. A. P. Nobrega, Y. Xin, H. R. Gutiérrez, *Adv. Funct. Mater.* **2018**, *28*, 1802949.
[39] S. M. Akkanen, H. A. Fernandez, Z. Sun, *Adv. Mater.* **2022**, *34*, 2110152.
[40] C. Hou, J. Deng, J. Guan, Q. Yang, Z. Yu, Y. Lu, Z. Xu, Z. Yao, J. Zheng, *Phys. Chem. Chem. Phys.* **2021**, *23*, 24579.
[41] H. Ardekani, R. Younts, Y. Yu, L. Cao, K. Gundogdu, *ACS Appl. Mater. Interfaces* **2019**, *11*, 38240.
[42] R. Rao, V. Carozo, Y. Wang, A. E. Islam, N. Perea-Lopez, K. Fujisawa, V. H. Crespi, M. Terrones, B. Maruyama, *2D Mater.* **2019**, *6*, 045031.
[43] S. V. Sivaram, A. T. Hanbicki, M. R. Rosenberger, G. G. Jernigan, H.-J. Chuang, K. M. McCreary, B. T. Jonker, *ACS Appl. Mater. Interfaces* **2019**, *11*, 16147.
[44] P. Atkin, D. W. M. Lau, Q. Zhang, C. Zheng, K. J. Berean, M. R. Field, J. Z. Ou, I. S. Cole, T. Daeneke, K. Kalantar-Zadeh, *2D Mater.* **2017**, *5*, 015013.
[45] H.-J. Kim, Y. J. Yun, S. N. Yi, S. K. Chang, D. H. Ha, *ACS Omega* **2020**, *5*, 7903.
[46] J. Lu, A. Carvalho, X. K. Chan, H. Liu, B. Liu, E. S. Tok, K. P. Loh, A. H. Castro Neto, C. H. Sow, *Nano Lett.* **2015**, *15*, 3524.
[47] X. Huang, Z. Li, X. Liu, J. Hou, J. Kim, S. R. Forrest, P. B. Deotare, *ACS Appl. Mater. Interfaces* **2021**, *13*, 44686.
[48] H. M. Oh, G. H. Han, H. Kim, J. J. Bae, M. S. Jeong, Y. H. Lee, *ACS Nano* **2016**, *10*, 5230.
[49] H. Zhang, J. R. Dunklin, O. G. Reid, S. J. Yun, S. U. Nanayakkara, Y. H. Lee, J. L. Blackburn, E. M. Miller, *Nanoscale* **2020**, *12*, 8344.
[50] L. Wang, M. Schmid, Z. N. Nilsson, M. Tahir, H. Chen, J. B. Sambur, *ACS Appl. Mater. Interfaces* **2019**, *11*, 19207.
[51] H. Qiu, T. Xu, Z. Wang, W. Ren, H. Nan, Z. Ni, Q. Chen, S. Yuan, F. Miao, F. Song, G. Long, Y. Shi, L. Sun, J. Wang, X. Wang, *Nat. Commun.* **2013**, *4*, 2642.
[52] P.-C. Shen, Y. Lin, C. Su, C. McGahan, A.-Y. Lu, X. Ji, X. Wang, H. Wang, N. Mao, Y. Guo, J.-H. Park, Y. Wang, W. Tisdale, J. Li, X. Ling, K. E. Aidala, T. Palacios, J. Kong, *Nat. Electron.* **2021**, *5*, 28.
[53] B.-K. Kim, T.-H. Kim, D.-H. Choi, H. Kim, K. Watanabe, T. Taniguchi, H. Rho, J.-J. Kim, Y.-H. Kim, M.-H. Bae, *npj 2D Mater. Appl.* **2021**, *5*, 9.
[54] B. Radisavljevic, A. Kis, *Nat. Mater.* **2013**, *12*, 815.
[55] O. Lopez-Sanchez, D. Lembke, M. Kayci, A. Radenovic, A. Kis, *Nat. Nanotech* **2013**, *8*, 497.
[56] Y.-C. Wu, C.-H. Liu, S.-Y. Chen, F.-Y. Shih, P.-H. Ho, C.-W. Chen, C.-T. Liang, W.-H. Wang, *Sci. Rep.* **2015**, *5*, 11472.
[57] P.-H. Chen, C.-A. Chen, Y.-T. Lin, P.-Y. Hsieh, M.-H. Chuang, X. Liu, T.-Y. Hsieh, C.-H. Shen, J.-M. Shieh, M.-C. Wu, Y.-F. Chen, C.-C. Yang, Y.-H. Lee, *ACS Appl. Mater. Interfaces* **2023**, *15*, 10812.

© 2024 The Author(s). Advanced Materials published by Wiley-VCH GmbH

15214095, 2025, 3, Downloaded from https://advanced.onlinelibrary.wiley.com/doi/10.1002/adma.202409825 by National Renewable Energy Lab, Wiley Online Library on [24/01/2025]. See the Terms and Conditions (https://onlinelibrary.wiley.com/terms-and-conditions) on Wiley Online Library for rules of use; OA articles are governed by the applicable Creative Commons License